Available online at www.sciencedirect.com
SCIENCE DIRECT®
Journal of Power Sources 140 (2005) 111–124
JOURNAL OF POWER SOURCES
www.elsevier.com/locate/jpowsour

Thermal analysis of lithium-ion batteries

S.C. Chen, C.C. Wan, Y.Y. Wang*

Department of Chemical Engineering, Tsing-Hua University, Hsin-Chu 300, Taiwan

Received 12 May 2004; accepted 19 May 2004
Available online 29 September 2004

Abstract

A detailed three-dimensional thermal model has been developed to examine the thermal behaviour of a lithium-ion battery. This model precisely considers the layered-structure of the cell stacks, the case of a battery pack, and the gap between both elements to achieve a comprehensive analysis. Both location-dependent convection and radiation are adopted at boundaries to reflect different heat dissipation performances on all surfaces. Furthermore, a simplified thermal model is proposed according to the examination of various simplification strategies and validation from the detailed thermal model. Based on the examination, the calculation speed of the simplified model is comparable with that of a one-dimensional model with a maximum error less than 0.54 K. These models successfully describe asymmetric temperature distribution inside a battery, and they predict an anomaly of temperature distribution on the surface if a metal case is used. Based on the simulation results from the detailed thermal model, radiation could contribute 43–63% at most to the overall heat dissipation under natural convection. Forced convection is effective in depressing the maximum temperature, and the temperature uniformity does not necessarily decrease infinitely when the extent of forced convection is enhanced. The metal battery case serves as a heat spreader, and the contact layer provides extra thermal resistance and heat capacity for the system. These factors are important and should be considered seriously in the design of battery systems.

Keywords: Thermal modelling; Thermal analysis; Lithium batteries; Heat dissipation; Thermal management

1. Introduction

The secondary lithium-ion battery with its high specific energy, high theoretical capacity and good cycle-life is a prime candidate as a power source for electric vehicles (EVs) and hybrid electric vehicles (HEVs). Safety is especially important for large-scale lithium-ion batteries, so thermal analysis is essential for their development and design. In order to provide sufficient capacity, a large-scale lithium-ion battery generally consists of many individual cells that are connected in parallel. This configuration inherently increases the thermal resistance of a battery, so thermal management becomes critical for operation.

Thermal modelling is an effective way to understand how the design and operating variables affect the thermal behaviour of the lithium-ion battery during charging and discharging. Bernardi et al. [1] have presented a general energy balance for battery systems. Chen and Evans [2–4] introduced several two-dimensional and three-dimensional thermal models. Lee et al. [5] also formulated a three-dimensional thermal model for electric vehicle batteries. These models were developed based on the transient heat-transfer equation and the heat generation equation proposed by Bernardi et al. [1]. The convective and radiative heat transfers on the surface were considered to be the boundary conditions, and the container of the battery was incorporated into a part of the boundary equations to facilitate the calculation. Pals and Newman [6] presented a one-cell model and a cell-stack model [7] to examine the effect of temperature variation on the heat-generation rate and the cell discharge behaviour. They showed that the heat-generation rate is much larger for lower temperatures than for higher temperatures. Song and Evans [8] also developed an electrochemical-thermal model,

* Corresponding author. Tel.: +886 3 571 3690; fax: +886 3 571 5408.
E-mail address: yywang@mx.nthu.edu.tw (Y.Y. Wang).

0378-7753/$ – see front matter © 2004 Elsevier B.V. All rights reserved.
doi:10.1016/j.jpowsour.2004.05.064

Nomenclature

A_1	sectional area of element 1 (m^2)
A_2	sectional area of element 2 (m^2)
C_p	heat capacity ($J\,kg^{-1}\,K^{-1}$)
$C_{p,i}$	heat capacity of specific element i ($J\,kg^{-1}\,K^{-1}$)
E	working voltage (V)
E_{oc}	open-circuit potential (V)
f	coefficient of Eq. (5) ($W\,m^{-2}\,K^{-n-1}$)
f_1	coefficient of Eq. (3) ($W\,m^{n-2}\,K^{-n-1}$)
f_2	coefficient of Eq. (4) ($J\,m^{-2}\,s^{-1/2}\,K^{-1}$)
h_c	convective heat transfer coefficient ($W\,m^{-2}\,K^{-1}$)
h_{comb}	combined heat transfer coefficient ($W\,m^{-2}\,K^{-1}$)
h_r	radiative heat transfer coefficient ($W\,m^{-2}\,K^{-1}$)
i	specific element i at the interface
I	total current (A)
k	effective thermal conductivity ($W\,m^{-1}\,K^{-1}$)
k_a	thermal conductivity of the case ($W\,m^{-1}\,K^{-1}$)
k_b	thermal conductivity of the contact layer ($W\,m^{-1}\,K^{-1}$)
k_X	thermal conductivity in X-direction ($W\,m^{-1}\,K^{-1}$)
k_Y	thermal conductivity in Y-direction ($W\,m^{-1}\,K^{-1}$)
k_Z	thermal conductivity in Z-direction ($W\,m^{-1}\,K^{-1}$)
k_ξ	thermal conductivity in X-, Y- or Z-direction ($W\,m^{-1}\,K^{-1}$)
k_1	thermal conductivity of element 1 ($W\,m^{-1}\,K^{-1}$)
k_2	thermal conductivity of element 2 ($W\,m^{-1}\,K^{-1}$)
L	characteristic length of the surface (m)
L_a	thickness of the case (m)
L_b	thickness of the contact layer (m)
L_1	length of element 1 (m)
L_2	length of element 2 (m)
n	coefficient of Eq. (3)
P	characteristic length (m)
Q	heat-generation rate per unit volume ($W\,m^{-3}$)
$\dot{Q}_c$	heat flux of convection ($W\,m^{-2}$)
$\dot{Q}_r$	heat flux of radiation ($W\,m^{-2}$)
S.D.	standard deviation
t	time (s)
T	temperature (K)
T_{avg}	average temperature of the system (K)
T_i	temperature of a specific control volume i (K)
$T_{i,ref}$	reference temperature of a specific control volume i (K)
T_s	the temperature of a specific point on the surface (K)
T_∞	the ambient temperature (K)
V	velocity of airflow ($m\,s^{-1}$)
V_i	volume of specific element i (m^3)
V_{total}	the total volume of the core region (m^3)
X	the coordinate along the direction of cell stacks
Y	the coordinate along the width direction
Z	the coordinate along the height direction

Greek symbols

ε	emissivity
ξ	X-, Y- or Z-coordinates of the Cartesian coordinate system (m)
ρ	density ($kg\,m^{-3}$)
ρ_i	density of specific element i ($kg\,m^{-3}$)
σ	Stefan–Boltzmann constant $5.67051E{-}8\,W\,m^{-2}\,K^{-4}$

which was coupled with a two-dimensional thermal model and a one-dimensional electrochemical model, to examine the relationship between thermal and electrochemical behaviour.

In order to obtain a precise simulation of the thermal behaviour of a battery, the geometry, configuration, physical, chemical and electrochemical properties should be delineated as accurately as possible in the model. It may be impractical to describe completely the complicated behaviour of a lithium battery with existing theoretical expressions. Besides, an unacceptable amount of calculation time could be required if the model is too complicated. Thus, it is common to adopt some simplified strategies such as neglecting the radiative heat transfer on the boundaries, taking the layered-structure of the cells as the homogeneous materials, transferring the container to be a part of the boundary equations, and degrading a three-dimensional system to a two-dimensional model. It should be recognized that proper assumptions greatly enhance the value of the thermal model, whereas any improper assumption can lead to inaccurate or incorrect simulation results. It is important to ascertain the critical factors that significantly affect the thermal behaviour and together with the minor elements that can be neglected in the thermal model. Hence, in the present work, a detailed thermal model has been developed to verify the correctness of the assumptions and to determine the optimal approach to simplify the thermal model. The manner in which battery design parameters and operating variables affect thermal behaviour is also analyzed.

2. Model development

2.1. Detailed three-dimensional thermal model

A schematic diagram of the rectangular lithium-ion battery is shown in Fig. 1. It is divided into three major portions, namely, the core region, the case, and the contact layer. The

Table 1
Value of coefficients used in Eq. (3) [9]

Geometry	Condition	f_1 (W m^{n-2} K^{-n-1})	f_1 (W in.$^{n-2}$ K^{-n-1})	n
Horizontal plate	Width >0.152 m (6 in.) upper surface $T_s > T_a$ or lower surface $T_s < T_a$	1.36133	0.0022	0.25
	Width >0.152 m (6 in.) upper surface $T_s < T_a$ or lower surface $T_s > T_a$	0.680665	0.0011	0.25
	Width <0.152 m (6 in.) upper surface $T_s > T_a$ or lower surface $T_s < T_a$	0.830233	0.0018	0.33
	Width <0.152 m (6 in.) upper surface $T_s < T_a$ or lower surface $T_s > T_a$	0.415117	0.0009	0.33
Vertical plate	Height >0.152 m (6 in.)	1.485088	0.0024	0.25
	Height <0.152 m (6 in.)	0.941145	0.0022	0.35

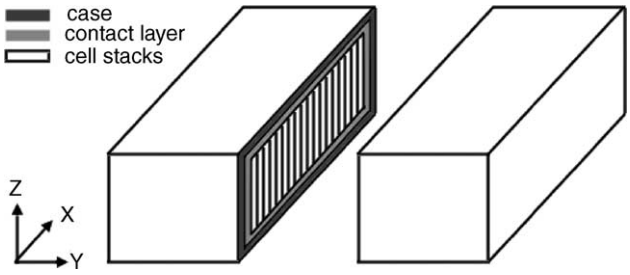

Fig. 1. Schematic representation of a typical lithium-ion battery.

core region consists of individual cells that are connected in parallel. Within an individual cell, the bi-cell configuration shown in Fig. 2 is one of the preferred designs and is chosen in this study. The case is the container of the battery. The contact layer stands for a narrow gap between the core region and the case, which is generally filled with liquid electrolyte.

In a lithium-ion battery, the liquid electrolytes are trapped in the pore structure of the electrodes, the separator, and the contact layers. The fluids tend to show limited mobility, so the contribution of convection to heat transfer inside the battery can be neglected. In addition, since the battery is an opaque system, the radiative heat transfer inside a battery is naturally insignificant. Therefore, the conductive heat transfer is the main mechanism inside a battery. The transient three-dimensional conductive heat transfer equation is as follows:

$$\rho C_p \frac{\partial T}{\partial t} = \frac{\partial}{\partial x}\left(k_X \frac{\partial T}{\partial x}\right) + \frac{\partial}{\partial y}\left(k_Y \frac{\partial T}{\partial y}\right) + \frac{\partial}{\partial z}\left(k_Z \frac{\partial T}{\partial z}\right) + Q \quad (1)$$

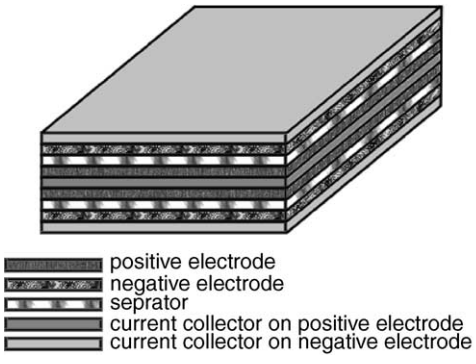

Fig. 2. Schematic diagram of a typical lithium-ion unit cell.

where ρ, C_p, k and Q are the density, heat capacity, thermal conductivity and heat-generation rate per unit volume, respectively. The definition of the coordinate system adopted in this study is shown in Fig. 1. It is worth mentioning that the four specified parameters in Eq. (1) may vary with location in the battery.

At the boundary, both convection and radiation must be considered. The convective heat transfer can be expressed as:

$$\dot{Q}_c = h_c(T_s - T_\infty) \quad (2)$$

where h, T_s and T_∞ denote the convective heat transfer coefficient, surface temperature and ambient temperature, respectively. It is important to know that T_s may vary with location, and h_c may be a function of both location and temperature. For natural convection, the convective heat-transfer coefficient can be determined in accordance with the following equation [9]:

$$h_c = f_1\left(\frac{|T_s - T_\infty|}{P}\right)^n \quad (3)$$

where P denotes the characteristic length of the surface, and f_1 and n are the coefficients summarized in Table 1. For forced convection, the convective heat transfer coefficient can be calculated by applying the following equation [9]:

$$h_c = f_2\sqrt{\frac{V}{L}} \quad (4)$$

where f_2, V and L are the temperature-dependent coefficient, the velocity of the airflow, and the characteristic length of the surface, respectively. The values of f_2 at several temperatures are listed in Table 2. The coefficient is weakly dependent on the average temperature, and can be treated as a constant value if the temperature variation is sufficiently small; hence, the average value of f_2 is applied in our work. Eqs. (3) and (4) are substituted in Eq. (2), and the following expressions

Table 2
Value of weakly temperature-dependent coefficient f_2 in Eq. (4) [9]

Average temperature T (K)	f_2 (J m^{-2} s$^{-1/2}$ K^{-1})
273.15	3.963703
298.15	3.873619
323.15	3.783535
348.15	3.748887
373.15	3.721169

are obtained:

$$\dot{Q}_c = h_c(T_s - T_\infty) = f|T_s - T_\infty|^n(T_s - T_\infty),$$

$$f = \frac{f_1}{P^n}, \quad \text{the value of } n \text{ is listed in Table 1 (natural convection),}$$

$$f = f_2\sqrt{\frac{V}{L}}, \quad n = 0 \text{ (forced convection)} \tag{5}$$

where f is the temperature-independent coefficient. In addition to the convective heat-transfer, the radiative heat transfer at the boundary is considered simultaneously in this model. The radiative heat transfer is expressed as follows:

$$\dot{Q}_r = \varepsilon\sigma(T_s^4 - T_\infty^4) \tag{6}$$

where ε and σ denote the emissivity and the Stefan–Boltzmann constant, respectively. Combining Eqs. (5) and (6), the boundary condition related to the convective and radiative heat transfer can be obtained as follows:

$$\begin{aligned} -k_\xi\frac{\partial T}{\partial \xi} &= \dot{Q}_c + \dot{Q}_r = h_{comb}(T_s - T_\infty) \\ &= [h_c + h_r](T_s - T_\infty) \\ &= [f|T_s - T_\infty|^n + \varepsilon\sigma(T_s^2 + T_\infty^2)(T_s + T_\infty)] \\ &\quad \times(T_s - T_\infty) \end{aligned} \tag{7}$$

where h_{comb} is the combined heat-transfer coefficient, and ξ can be X-, Y- or Z-coordinates. The main advantage of restructuring the boundary equation to Eq. (7) is that it facilitates the numerical operation.

In addition, we need to determine the heat-generation rate of a lithium-ion battery during operation. The following heat-generation equation developed by Bernardi et al. [1] is adopted:

$$Q = \frac{I}{V_{total}}\left(E_{oc} - E - T\frac{dE_{oc}}{dT}\right) \tag{8}$$

where I, V_{total}, E_{oc} and E denote the total current of the battery, the total volume of the core region, the open-circuit potential and the working voltage, respectively. This equation is efficient enough so that full attention can be paid to detailed thermal analysis. The limitation is that the potential terms in Eq. (8) should be obtained, and the effect of temperature on electrochemical behaviours cannot be evaluated [6–8,10]. In fact, a model focused on electrochemical analysis can adopt a more rigorous electrochemical model [11] here to predict theoretically the heat-generation rate. On the other hand, simplifying such a complicated model to speed up the calculation is critical, and the simulation results may be unreliable if the simplification strategy is not validated with a detailed model.

Finally, it is necessary to determine several physical parameters at the interfaces between the different components inside a lithium-ion battery. In the numerical analysis, these parameters are applied when the control volume is across the interface. The product value of density and heat capacity is calculated based on the volume of each component as follows:

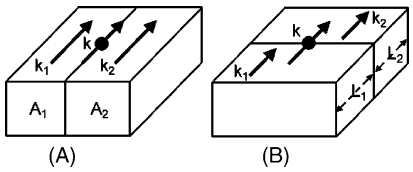

Fig. 3. Schematic representation of the effective thermal conductivity at the interface. The elements are connected in (A) parallel; (B) series.

$$\rho C_p = \frac{\sum_i \rho_i C_{p,i} V_i}{\sum_i V_i} \tag{9}$$

where V denotes the volume of a specific component. The thermal conductivity at the interface should be determined based on connection between components and the contact resistance of the interface. Fortunately, the effect of contact resistance on effective thermal conductivity is insignificant in this case, because most of the pores and gaps are filled with liquid electrolyte, and the thermal conductivity of the liquid electrolyte is comparable with that of the materials, such as the separator and the electrode, in the core region. When the elements are connected in series, the thermal conductivity is determined by:

$$k = \frac{L_1 + L_2}{(L_1/k_1) + (L_2/k_2)} \tag{10}$$

and the following equation is applied when the elements are in parallel:

$$k = \frac{A_1}{A_1 + A_2}k_1 + \frac{A_2}{A_1 + A_2}k_2 \tag{11}$$

The notations in these two equations are illustrated in Fig. 3. A complicated case with a combination of series and parallel elements can be also evaluated based on Eqs. (10) and (11). Because the control volume is extremely small in comparison with the volume of each component, adopting the above equations to estimate the physical properties works well.

Having developed the model for lithium-ion batteries, suitable numerical techniques for computation, were chosen using finite-difference technique to discretize the mathematical model. In order to obtain maximum flexibility, a variable grid-size system was developed instead of the conventional constant grid-size system. In addition, a plane iteration procedure was derived to improve the convergence speed. This program was based on a multi-thread architecture; hence, it can calculate simultaneously on parallel processors.

In the detailed thermal model, there are no additional assumptions and simplifications for the core region, the contact layer, and the case. It can avoid the risk of getting unreliable simulation results due to improper assumptions and simplifications. The extent of convection determined automatically based on the formulae is obviously more reliable than that specified arbitrarily. The effect of convection and radiation

Table 3
Detailed information of simplified thermal models to be examined

Number	Dimension	Core region	Case and contact layer	Radiation
1	1D (*X*)	*X*: considering the layered-structure; *Y*, Z: ignored	*X*: considered; *Y*, *Z*: ignored	Considered
2	1D (*Y*)	*Y*: taking the average property; *X*, *Z*: ignored	*Y*: considered; *X*, *Z*: ignored	Considered
3	1D (*Z*)	*Z*: taking the average property; *X*, *Y*: ignored	*Z*: considered; *X*, *Y*: ignored	Considered
4	2D (*X*, *Y*)	*X* and *Y*: considering the layered-structure; *Z*: ignored	*X*, *Y*: considered; *Z*: ignored	Considered
5	2D (*X*, *Z*)	*X* and *Z*: considering the layered-structure; *Y*: ignored	*X*, *Z*: considered; *Y*: ignored	Considered
6	2D (*Y*, *Z*)	*Y* and *Z*: taking the average property; *X*: ignored	*Y*, *Z*: considered; *X*: ignored	Considered
7	3D (*X*, *Y*, *Z*)	Considering the layered-structure	Ignored	Considered
8	3D (*X*, *Y*, *Z*)	Considering the layered-structure	Transferred to boundary conditions	Considered
9	3D (*X*, *Y*, *Z*)	Considering the layered-structure	Considered	Ignored
10	3D (*X*, *Y*, *Z*)	Taking the average property	Considered	Considered
11	3D (*X*, *Y*, *Z*)	Considering the layered-structure	Considered	Considered

Number 11 is a detailed thermal model, which is taken as a reference for the simulation.

are evaluated simultaneously, so that the heat dissipation on the surface can be properly calculated. Furthermore, coupling the model with the flexible numerical techniques, it is possible to simulate a lithium-ion battery integrated with any heat dissipation device. Adoption of this model provides detailed simulation results that are consistent with the physical meanings, and that cannot be predicted by other models.

2.2. Simplified three-dimensional thermal model

From a practical point of view, both accurate and efficient calculations are essential. The detailed thermal model developed here is focused on scientific applications, and it may not be the best candidate to perform the practical simulation due to its inefficient calculation. How to apply the suitable assumption and simplification is the main challenge to develop a proper simplified thermal model. Fortunately, the systematic simplification can be progressed by evaluating the validity of the assumptions with the detailed thermal model. Therefore, the accuracy of a simplified model can be guaranteed.

The strategies used to simplify the thermal model are summarized in Table 3. Numbers 1–3 degrade a complicated three-dimensional phenomenon to a one-dimensional model, which greatly facilitates the calculation, although the loss of accuracy should be examined carefully. Note that Number 1 considers the layered-structure of the core region without simplification, whereas Numbers 2 and 3 are compelled to adopt the average properties of the core region, because a one-dimensional model focused on only *Y*- or *Z*-coordinates is not sufficient to describe the layered-structure along the *X*-coordinate. The average properties of the core region along *Y*- and *Z*-coordinates are calculated based on Eq. (9) and the following equation.

$$k = \frac{\sum_i A_i k_i}{\sum_i A_i} \tag{12}$$

A two-dimensional model has improved the accuracy over a one-dimensional model, but it is expected to expend more time on calculation. Numbers 4–6, which neglect *Z*-, *Y*- and *X*-coordinates respectively, are two-dimensional models that are examined here. Note that for the same reason discussed above, Number 6 takes the average property instead of considering the layered-structure of the core region.

Number 7 is a three-dimensional thermal model that focuses on analysis of the core region. It ignores the effects of the case and the contact layer on heat transfer, so the calculation of this model is much faster than a detailed three-dimensional thermal model. Nevertheless, the correctness of this assumption should be verified. Instead of neglecting the case and the contact layer, Number 8 adopts a strategy to incorporate these components to parts of the boundary conditions. It requires nearly the same amount of time as Number 7 to calculate the results, but an improvement in accuracy may be achieved. The technique to transfer these components to parts of the boundary conditions is analogous to that proposed by Chen and Evans [3,4] as follows:

$$h_{\text{comb}} = \frac{1}{(1/(h_c + h_r)) + (L_a/k_a) + (L_b/k_b)} \tag{13}$$

where L_a, k_a and L_b, k_b denote the thickness and the thermal conductivity of the case and the contact layer, respectively. The major problem in adopting this formula is that it ignores the contribution of the case and the contact layer to the total heat capacity, and also neglects the heat flows that are parallel to the surface. Number 9 is also a simplified three-dimensional thermal model that neglects the non-linear radiation effect under the boundaries. Improvement in the calculating speed and the accuracy of the results should be further examined.

An optimum technique to simplify a three-dimensional thermal model is also proposed, as described in Number 10. The battery case and the contact layer appear to play significant roles in heat dissipation, and ignoring these components does not significantly improve the calculating speed. Hence, the case and the contact layer are not simplified further. The evaluation of the core region generally takes most of the calculation time, so that simplifying this region may be the best strategy. The core region is composed of repeating cells, and each cell consists of several extremely thin layers. It is assumed that the thermal behaviour of the core region is analogous to that of a homogeneous material, and the cor-

Table 4
Thermal and physical properties of each material used in the simulation

Material	Density (kg m^{-3})	Heat capacity (J kg^{-1} K^{-1})	Thermal conductivity (W m^{-1} K^{-1})	Emissivity
Carbonaceous electrode	1347.33[a]	1437.4[a]	1.04[a]	
$LiCoO_2$ electrode	2328.5[a]	1269.21[a]	1.58[a]	
Al foil	2702 [12]	903 [12]	238 [12]	
Cu foil	8933 [12]	385 [12]	398 [12]	
PP separator	1008.98[a]	1978.16[a]	0.3344[a]	
Al-2024	2770 [12]	875 [12]	170 [12]	0.25 (oxidized) [12]; 0.4 (rough) [12]
S. S. AISI-304	7900 [12]	477 [12]	14.6 [12]	
Liquid electrolyte	1129.95[a]	2055.1[a]	0.60[a]	

Porous materials such as the electrodes and the separator were soaked in the electrolyte before testing.
[a] From experiment.

responding homogeneous properties of the layered-structure can be obtained by adopting Eqs. (9) and (12) as well as the following equation.

$$k = \frac{\sum_i L_i}{\sum_i (L_i / k_i)} \tag{14}$$

The thermal conductivity along the *X*-coordinate is calculated by Eq. (14), and that along the *Y*- and *Z*-coordinate by Eq. (12). By transferring the layered-structured core region to a homogeneous material, the complicated calculation can be avoided, so the calculation time may be reduced significantly because the total grids in the numerical analysis are reduced.

In order to determine the accuracy and efficiency of these simplified thermal models, the thermal behaviour of a 185.3 Ah large-scale lithium-ion battery is simulated by these 10 models plus the reference model, Number 11, which is the detailed thermal model that has been previously proposed. The detailed information on the battery and the simulation is summarized in Tables 4–6. The experimental results on cell potential as a function of utilization at different discharge rates, which is one of the inputs of the simulation, are shown in Fig. 4. Note that the physical properties listed in Table 4 are the values of the composite components instead of the intrinsic values of each material.

The accuracy for each simplified thermal model is evaluated quantitatively by four representative indexes, namely: the absolute deviation of maximum temperature, the minimum temperature, the average temperature, and the standard deviation of the temperature distribution at the end of discharge. The maximum temperature is important for secure design, the minimum temperature is easy to measure from the surface, the average temperature indicates the total heat left in the system, and the standard deviation evaluates the degree of consistency for the temperature profile. All of these four factors are meaningful and are chosen to be the indexes of accuracy. The reference results are from the detailed thermal model Number 11. The standard deviation (S.D.) of the temperature distribution is calculated by means of the following

Table 5
Information of battery and setting of simulation

Size of battery	19.32 cm × 10.24 cm × 10.24 cm
Size of each unit cell	0.0636 cm × 10 cm × 10 cm
Size of core region	19.08 cm × 10 cm × 10 cm
Thickness of the contact layer	0.05 cm
Thickness of the Al foil	0.002 cm
Thickness of the PP separator	0.0035 cm
Thickness of the Cu foil	0.0014 cm
Thickness of the case	0.07 cm
Thickness of positive electrode	0.014 cm
Thickness of negative electrode	0.0116 cm
Theoretical capacity	185.3 Ah
Ambient temperature	300 K
dE_{oc}/dT	0.00022 V K^{-1} [2]
Initial temperature	300 K

Table 6
Setting of simulations I and II for each thermal model

	Simulation I	Simulation II
Convection type	Natural convection	Forced convection
Heat transfer coefficient	Generated from the model dynamically	100 W m^{-2} K^{-1}
Emissivity	0.25	0.25
Discharge rate	3*C*	3*C*
Notation of simulations	Prefix 'N' + ID number (see Table 3) (e.g. N1, N2, N3, . . .)	Prefix 'F' + ID number (see Table 3) (e.g. F1, F2, F3, . . .)

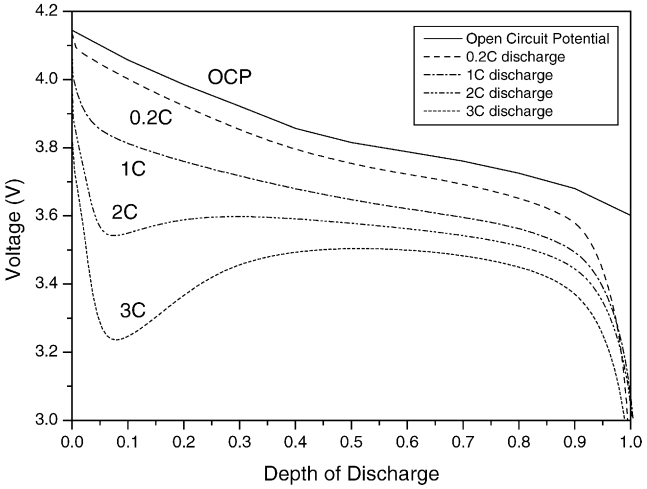

Fig. 4. Experimental results about the cell potential as a function of utilization for the simulated battery. The experiment is supported by Industrial Technology Research Institute (ITRI), and is proceeded at constant ambient temperature 300 K.

Table 7
Simulation results of simplified thermal models at end of 3*C* discharge

ID	Deviation of maximum temperature (K)	Deviation of minimum temperature (K)	Deviation of average temperature (K)	Standard deviation of temperature profile (K)	Deviation index	Time index
Natural convection (N)						
N1	9.516 (15.34%)	3.326 (6.03%)	9.095 (15.13%)	9.31	7.20	88.72
N2	4.997 (8.05%)	10.352 (18.75%)	6.615 (11.00%)	6.67	6.91	1.00
N3	4.864 (7.85%)	9.64 (17.46%)	6.437 (10.70%)	6.50	6.65	1.07
N4	4.566 (7.37%)	2.543 (4.61%)	4.391 (7.30%)	4.44	3.88	810.02
N5	4.436 (7.15%)	2.723 (4.93%)	4.218 (7.01%)	4.29	3.85	2610.07
N6	0.726 (1.17%)	5.28 (9.57%)	2.058 (3.42%)	2.39	2.08	2.79
N7	3.232 (5.21%)	0.316 (0.57%)	3.292 (5.47%)	3.33	1.83	3085.80
N8	3.277 (5.28%)	0.204 (0.37%)	3.353 (5.58%)	3.36	1.66	3085.80
N9	1.223 (1.97%)	2.394 (4.34%)	1.455 (2.4%)	1.47	1.58	14370.15
N10	0.005 (0.01%)	0.338 (0.61%)	−0.006 (−0.01%)	0.03	0.02	22.14
N11	Ref.	Ref.	Ref.	0.00	0.00	14370.15
Forced convection (F)						
F1	40.846 (133.10%)	8.686 (60.22%)	36.680 (141.27%)	37.94	26.51	80.40
F2	15.263 (49.73%)	24.151 (167.42%)	18.535 (71.38%)	18.64	18.89	1.00
F3	15.263 (49.73%)	24.151 (167.42%)	18.535 (71.38%)	18.64	18.89	1.00
F4	14.519 (47.31%)	4.145 (28.73%)	12.741 (49.07%)	13.11	10.01	1116.03
F5	14.519 (47.31%)	4.145 (28.73%)	12.741 (49.07%)	13.11	10.01	1116.03
F6	0.845 (2.75%)	10.348 (71.74%)	3.625 (13.96%)	4.61	3.48	2.73
F7	−0.024 (−0.08%)	−3.484 (−24.16%)	0.279 (1.08%)	7.47	0.65	3882.46
F8	0.656 (2.14%)	−3.41 (−23.64%)	0.985 (3.79%)	1.42	1.33	3882.46
F9	0.273 (0.89%)	0.795 (5.51%)	0.203 (0.78%)	0.26	0.33	11220.31
F10	−0.013 (−0.04%)	0.541 (3.75%)	−0.075 (−0.29%)	0.06	0.07	17.57
F11	Ref.	Ref.	Ref.	0.00	0.00	11929.74

Values in parentheses denote relative deviation.

equation:

$$\text{S.D.} = \sqrt{\frac{\sum_{i=1}^{n} V_i (T_i - T_{i,\text{ref}})^2}{V_{\text{total}}}} \quad (15)$$

where T_i and $T_{i,\text{ref}}$ denote the temperature of a simplified model and that of the detailed model at a specific location, respectively.

The efficiency of each simplified thermal model is evaluated by examining the user time for each program to complete the simulation [13]. The calculation is terminated when the maximum error of temperature is less then 10^{-8} K. In order to evaluate the performance fairly, the same numerical technique (implicit finite-difference technique) is adopted, the advantageous algorithm is applied, and the minimum allowable number of grids is used for each model. The calculation performance of each simplified model is strongly dominated by the complicity of algorithms, although the programming skill affects the efficiency as well. The results are normalized base on the most efficient model (generally Number 2), because the user time for a specific program depends on the organization of computers, and the absolute value is meaningless to recognize the efficiency.

The simulation results are summarized in Table 7. Note that the comparison between the models is restricted to the core region, because some of the simplified models neglect the case and the contact layer. Due to the identity of the boundary conditions, F2 and F3 as well as F4 and F5 are equivalent, so that the simulation does not repeat. In order to compare

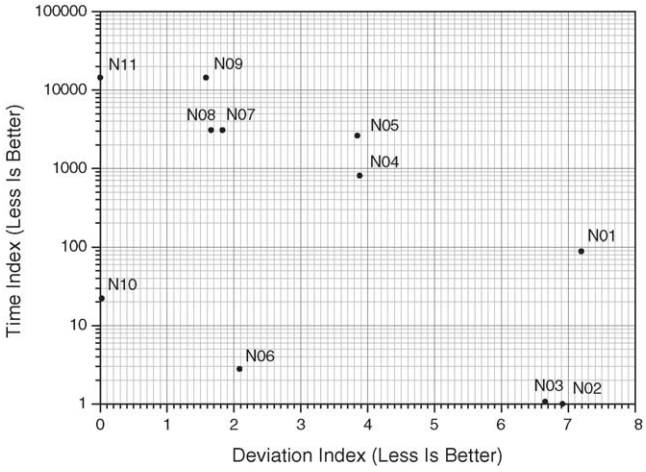

Fig. 5. Deviation index and time index of simplified thermal models under natural convection.

the accuracy of the simplified models systemically, a single index named deviation index is adopted; it is the geometric mean of four representative factors described above. The performance of each simplified thermal model under natural and forced convection is given in Figs. 5 and 6, respectively. With a smaller deviation index and time index, the model performs better. The models fall into the lower left corner, which indicates that both are accurate and efficient.

According to the results, it is found that a one-dimensional model is insufficient to represent the thermal behaviour, especially for the battery under forced convection. Furthermore, a

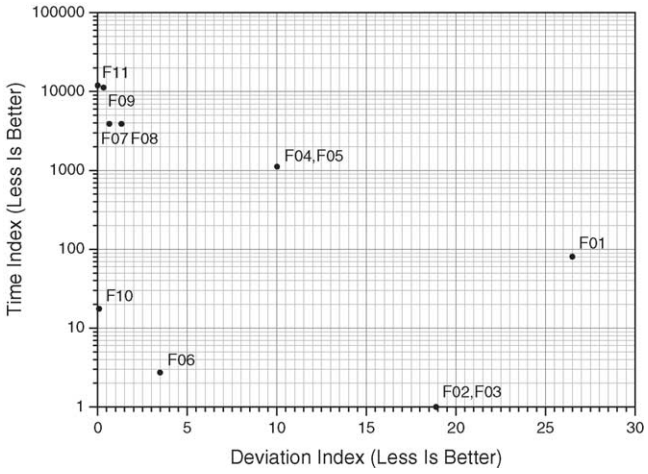

Fig. 6. Deviation index and time index of simplified thermal models under forced convection (h = 100 W m^{-2} K^{-1}).

one-dimensional model focused on *Y*- or *Z*-coordinates provides better accuracy and is about 85 times more efficient than that focused on the *X*-coordinate. Thus, it is clearly important to select the proper coordinate to analyze. It also suggests that the heat transfer along the *Y*- and *Z*-coordinates is more significant than that along the *X*-coordinate.

As expected, two-dimensional models provide better accuracy but consume more time than one-dimensional models. It is especially impressive that the Number 6 simplified model provides both good accuracy and efficiency. By neglecting the complicated layered-structure along the *X*-coordinate and adopting the average properties at the *Y*- and *Z*-coordinates, it is 200–1000 times more efficient than Numbers 4 and 5. It wisely does not analyze the *X*-coordinate, which is the most inefficient direction for heat transfer, so that the accuracy of Number 6 is much better than that of Numbers 4 and 5.

Three-dimensional thermal models provide the best accuracy, although the calculation time is expanded to 3000–11,000 times that of the one-dimensional models. The only exception is Number 10, which is the optimum simplification proposed here. Inspection of the results shows that Number 8, which transfers the case and the contact layer into part of the boundary conditions, is more accurate than Number 7 under natural convection, although the opposite result is obtained under forced convection. This indicates that transferring the case and the contact layer into part of the boundary conditions may not be better than simply neglecting these two components. This is because it may be dangerous to neglect the contribution of the heat capacity and the heat flow parallel to the surface within the case and the contact layer.

Number 9 is a detailed thermal model that does not consider the radiation. Although the emissivity of these simulations is only 0.25, it was found that the deviation is significant under natural convection, and is insignificant under forced convection. This result is consistent with the fact that the contribution of radiation is conspicuous when the system is under weak convection. Neglecting the radiation does not improve the calculating efficiency significantly, so that the detailed thermal model, Number 11, can fully replace Number 9.

Number 10 gives nearly the same accuracy as the detailed three-dimensional thermal model, Number 11, but the calculating efficiency is better than the one-dimensional model, Number 1. Accordingly, it is a good strategy to take the average property of the core region to avoid the complicated computation of the layered-structure. This means that the layered-structured core region behaves as a homogeneous material under heat transfer. In practice, this model is as good as the detailed thermal model to predict the asymmetric temperature profile and the anomaly of temperature distribution on the surface (see Sections 3.2 and 3.3), which cannot be achieved by other simplified models.

After discussion, it is concluded that Number 10 is the best simplified thermal model for both accuracy and efficiency. It provides nearly the same accuracy as a detailed model, but is about 660 times faster. Neglecting the most inefficient *X*-coordinate for heat transfer, such as that of Number 6, to degrade a three-dimensional system to a two-dimensional model can further increase the calculating efficiency (about seven times faster than Number 10) with acceptable deviation. This may be applicable to situations where the computation efficiency is extremely important.

3. Results and discussion

The thermal behaviour of a typical large-scale lithium-ion battery is examined in accordance with the detailed thermal model proposed here. Information on the simulation is summarized in Tables 4 and 5. The default value of emissivity is 0.25, and the natural convection with radiation is the default condition at the boundaries. The cell potential as a function of utilization at different discharge rates, which is obtained from the experiment, is shown in Fig. 4. The simulation is terminated when the maximum error in temperature is less than 10^{-8} K. Except for the additional declaration in the following paragraph, the simulation always follows the setting described above.

3.1. Temperature variation under galvanostatic discharge

The temperature variation under 3*C*, 2*C* and 1*C* galvanostatic discharge with natural convection and simple radiation is shown in Fig. 7. The average temperature is calculated in accordance with the following equation.

$$T_{\text{avg}} = \frac{\sum_i V_i T_i}{\sum_i V_i} \tag{16}$$

The maximum temperature increases and the temperature uniformity decreases on increasing the discharge rate significantly. This means that thermal control is critically important when the battery undergoes high-rate discharge.

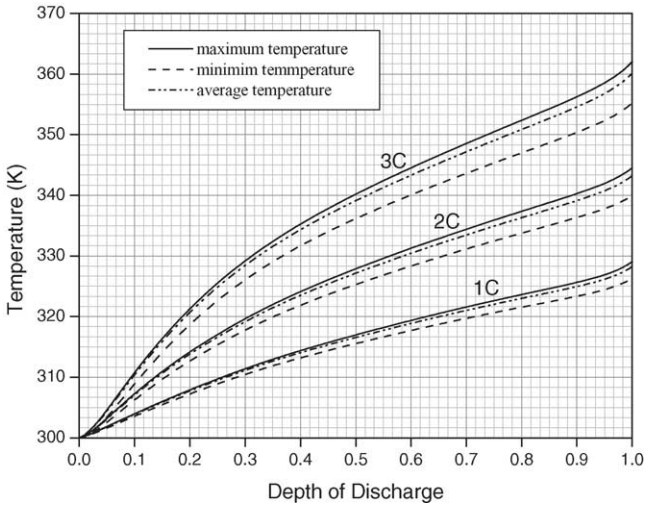

Fig. 7. Maximum temperature, minimum temperature, and volume averaged temperature at 3*C*, 2*C*, and 1*C* discharge rate.

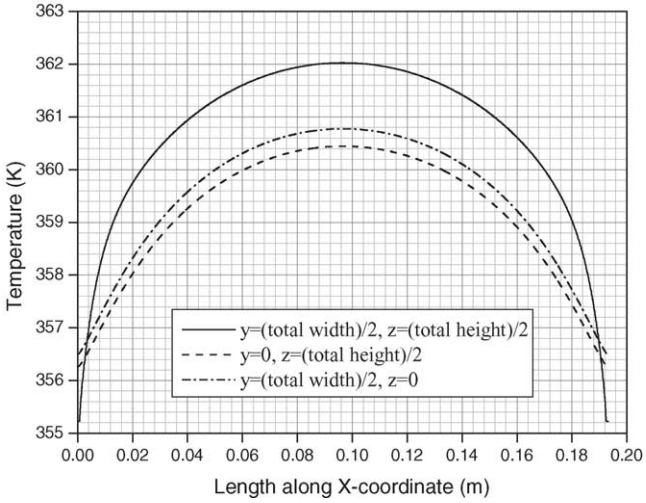

Fig. 8. Temperature distribution along the *X*-coordinate at the end of the 3*C* discharge procedure.

3.2. Temperature distribution and thermal resistance within battery

Before presenting the results, it is useful to consider the likely temperature distribution in a lithium-ion battery. The core region is the heat source of the lithium-ion battery during the operation; hence, common sense would dictate that the maximum temperature should occur at the center of the battery. Temperature distribution is not symmetrical, however, since natural convection is more efficient on the top surface than on the bottom surface when the surface temperature is higher than the ambient temperature [9,12]. Therefore, it is reasonable to expect that the maximum temperature should occur slightly below the center of the battery. Moreover, the effective thermal conductivity of the core region, which can be evaluated from Eqs. (12) and (14), is better in the *Y*- and *Z*-directions (24.840 $W m^{-1} K^{-1}$) than in the *X*-direction (1.035 $W m^{-1} K^{-1}$). Although the calculation of effective thermal conductivity is based on the thermal resistance, and it may not predict accurate results, it indicates that the temperature distribution will be more uniform in the *Y*- and *Z*-directions than in the *X*-direction.

The temperature distribution along the *X*-, *Y*- and *Z*-coordinates at the end of 3*C* discharge is shown in Figs. 8–10, respectively. The solid lines represent the temperature distribution along the centerline of the battery, and the dashed lines represent the temperature distribution on the surface. Inspecting the solid lines, the temperature distribution in the *X*-direction is much steeper than that in the *Y*- and *Z*-directions, so that the thermal resistance along the cell stacks is much larger than that parallel to the cell stacks. Due to the poor thermal conductivity of the contact layer and the excellent thermal conductivity of the case, these regions exhibit very steep and very gentle temperature gradients, respectively; hence, the temperature distribution across these components is easy to find in these solid lines.

The effect of the contact layer is more significant in the *Y*- and *Z*-directions than in the *X*-direction, as shown in Figs. 8–10, because the effective thermal conductivity in the *X*-direction is poor (1.035 $W m^{-1} K^{-1}$) and is comparable with that of the contact layer (0.6 $W m^{-1} K^{-1}$). Moreover, from the solid line in Fig. 10, it is seen that the temperature distribution along the *Z*-direction is asymmetrical. This result is consistent with the physical meaning discussed above.

3.3. Temperature distribution on the surface

Both of the dashed lines exhibit less sharp temperature gradient than the solid line in Figs. 8–10 due to the excellent thermal conductivity of the metal case. According to Fig. 8, the temperature on the surface (dashed lines) is lower than the temperature at the centerline (solid line) in most of the region, but the opposite phenomenon can be found on the two sides.

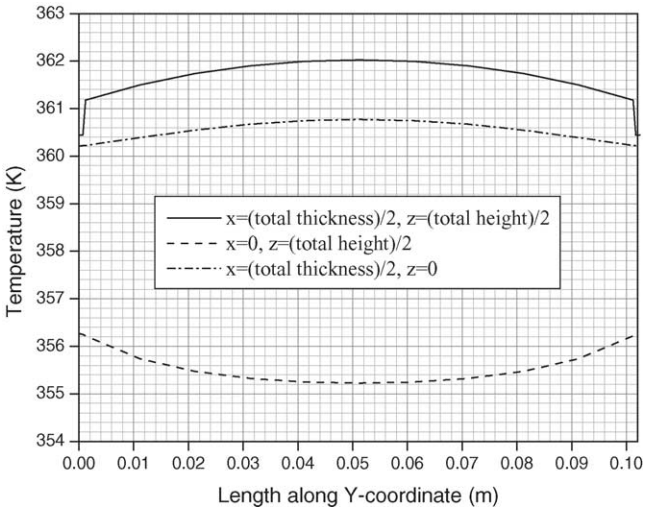

Fig. 9. Temperature distribution along the *Y*-coordinate at the end of the 3*C* discharge procedure.

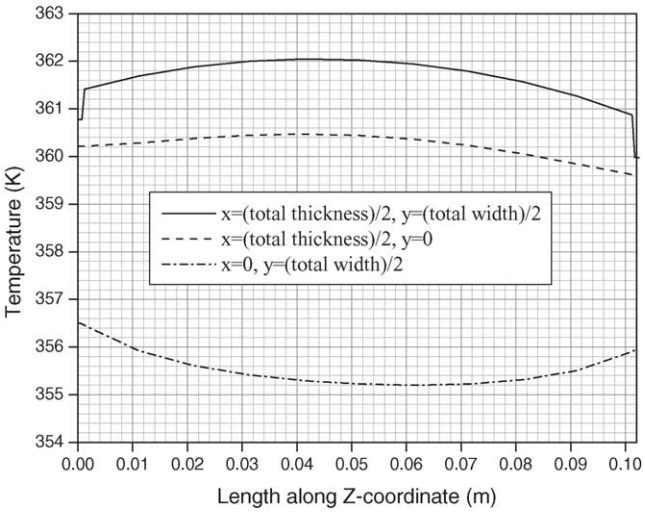

Fig. 10. Temperature distribution along the *Z*-coordinate at the end of the 3*C* discharge procedure.

Since the core region exhibits a large thermal resistance in the *X*-direction, whereas the metallic container displays excellent thermal conductivity in the same direction. Although in the interior regions, the temperature on the surface is lower than that at the centerline, the excellent thermal conductivity of the case offers a shortcut for heat to flow from the high temperature region to the low temperature region, so that a gentle temperature gradient is maintained on the surface. By contrast, the high thermal resistance in the *X*-direction of the core region depresses heat flow, whereby a steep temperature gradient is formed inside the battery. Therefore, an unusual phenomenon occurs on both sides of the battery, and it is easy to realize why the temperature in the central region of the surfaces $X = 0$ and $X = X'$ is lower than the temperature around it, as shown in Figs. 9 and 10. It is worth noting that the phenomenon discussed above occurs only in the *X*-direction, because the thermal conductivity in the *Y*- and *Z*-directions of the core region is sufficiently large to prevent the temperature distribution anomaly discussed above. The contours of

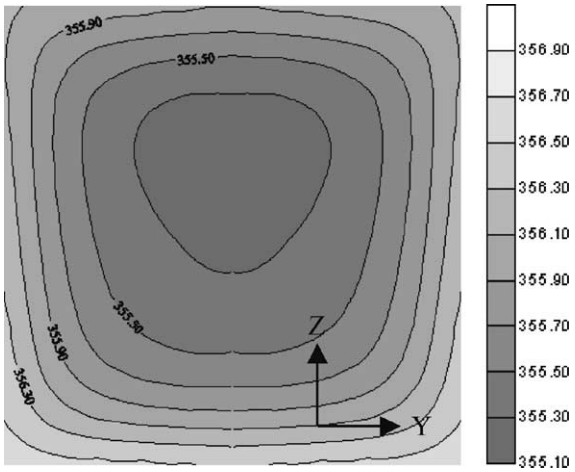

Fig. 12. Temperature distribution on the surface $X = 0$ at the end of 3*C* discharge procedure. There is a local minimum temperature on the surface.

the temperature distribution on the surface $Y = 0$ and $X = 0$ are shown in Figs. 11 and 12, respectively, and the phenomena discussed above becomes apparent.

The data discussed above clearly indicates that both the contact layer and the case strongly affect the temperature distribution in a lithium-ion battery, and that the temperature distribution inside the battery may different from that on the surface. This is why the simplified thermal models that do not properly deal with these two components fail to predict the phenomena discussed above, and they always predict the symmetrical and convex temperature distribution. In fact, only the detailed thermal model and the simplified thermal model, Number 10, are able to predict accurate results that are consistent with the physical meanings.

3.4. Heat dissipation mechanism on surface

In this model, the boundary conditions for convection and radiation are generated automatically according to the temperature on the surface and the conditions of the surroundings.

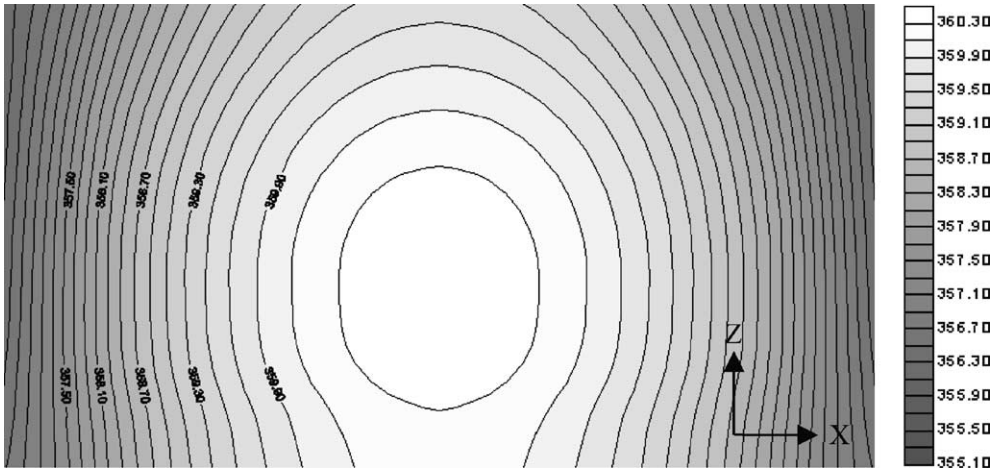

Fig. 11. Temperature distribution on the surface $Y = 0$ at the end of 3*C* discharge procedure. There is a local maximum temperature on this surface.

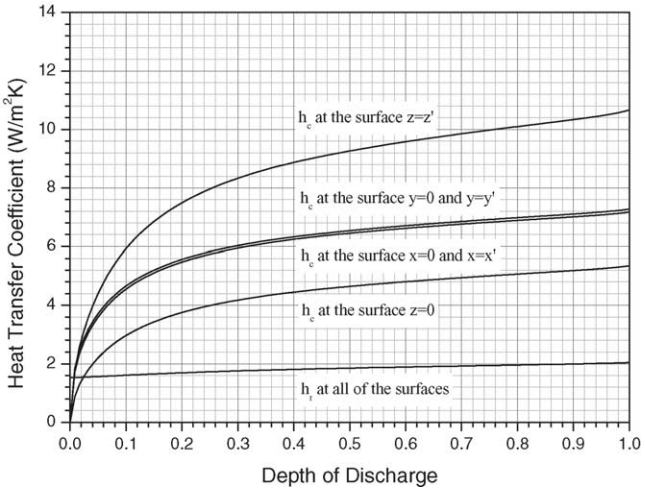

Fig. 13. Variation of convective and radiative heat transfer coefficient at 3*C* discharge rate with the emissivity to be 0.25. These values are calculated based on the average temperature on each surface.

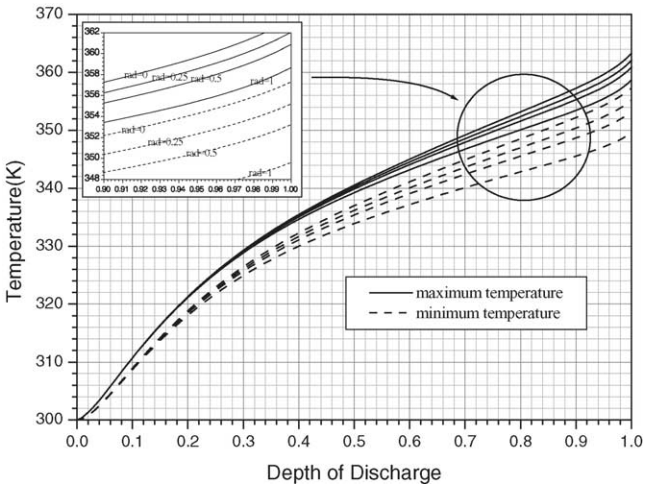

Fig. 14. Temperature variation at 3*C* discharge rate with different emissivity on the surface.

In comparison with the constant heat-transfer coefficient arbitrarily specified on the boundary as commonly used, this is closer to reality. The heat-transfer coefficient is undetermined until the simulation is finished; hence, it is worth investigating the convective and radiative effects on each surface after the simulation is completed. The variation in the convective and radiative heat-transfer coefficients when the battery is under 3*C* discharge with natural convection is shown in Fig. 13. The heat transfer coefficients are calculated according to the average temperature on each surface. The radiative heat-transfer coefficients on all surfaces are very close to each other; therefore, they overlap to a single curve. The top surface (at $Z = Z'$) exhibits the highest convective heat transfer, and the bottom surface (at $Z = 0$) gives the worst, as expected. It is surprising that the radiative heat transfer contributes about 16–18, 22–24 and 28–30% to the total heat transfer on the top surface, the vertical surfaces and the bottom surface, respectively. It is worth noting that the value of emissivity is specified to be only 0.25 in the simulation, yet it shows a significant contribution. This implies that radiative heat transfer cannot be omitted when the battery is operated with natural convection; and it is why the simplified model, Number 9, cannot work well when the battery is under natural convection.

3.5. Effect of radiation on heat transfer

After analyzing the heat dissipation mechanism on the surface, the effect of radiative heat transfer by varying the surface emissivity has been examined, as shown in Fig. 14. Taking the white body as the reference state, the maximum temperature at the end of discharge decreases by 1.22, 2.60 and 4.60 K, and the minimum temperature decreases by 2.10, 4.07 and 7.68 K for the emissivity at 0.25, 0.5 and 1, respectively. This again demonstrates that radiative heat transfer plays an important role in heat dissipation, and it cannot be ignored in calculations. In addition, it is clear that the decrease in the minimum temperature is much larger than that for the maximum temperature, due to the radiative effect on the surface.

The variation of convective and radiative heat transfer for a black body is shown in Fig. 15. Compared with Fig. 13, the contribution of radiative heat transfer to the total heat dissipation rises to between 43 and 63% for each surface with a slight decrease in convective heat transfer. Therefore, the heat dissipation would be enhanced by improving the emissivity with proper surface treatment on the battery case.

3.6. Effect of forced convection on heat transfer

Forced convection is employed whenever possible since it generally offers much better heat transfer than natural convection. In order to examine the effectiveness of forced convection, a battery with additional forced convection under 3*C* discharge is simulated.

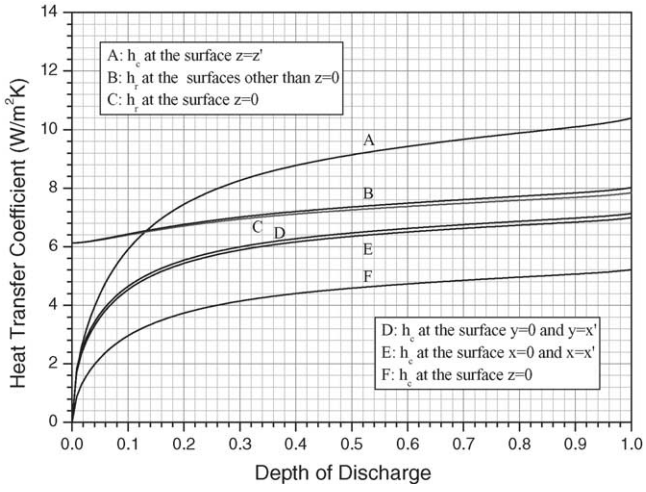

Fig. 15. Variation of convective and radiative heat transfer coefficient at 3*C* discharge rate with the emissivity fixed at unity.

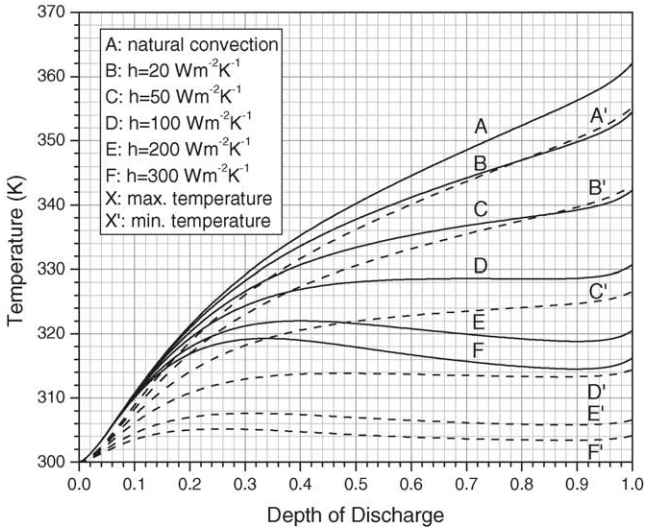

Fig. 16. Temperature variation under different convection conditions at 3*C* discharge rate.

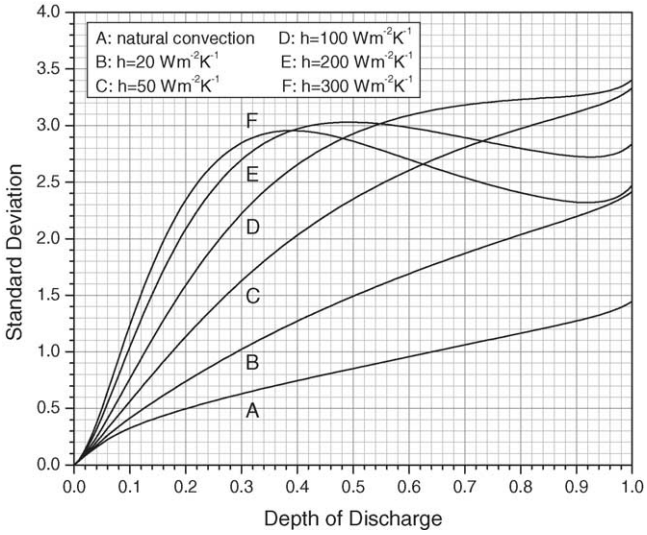

Fig. 17. Standard deviation of temperature among the whole system under different extent of convection.

The temperature variation under 3*C* discharge with different convection conditions is plotted in Fig. 16. Taking the simulation results from natural convection as the reference state, the maximum temperature decreases by 7.58, 19.75, 31.36, 41.56 and 45.84 K, and the minimum temperature decreases by 12.07, 28.61, 40.78, 48.58 and 51.08 K for a convective heat-transfer coefficient set at 20, 50, 100, 200 and 300 $\mathrm{W\,m^{-2}\,K^{-1}}$, respectively. Obviously, enhancing the forced convection greatly depresses both the maximum temperature and the minimum temperature in the system, and it leads to the same result that the decrease of minimum temperature is larger than that for the maximum temperature, as discussed in the previous section. Note that the effectiveness of enhancing the forced convection to increase the heat dissipation is much more significant when the system has low to moderate convection, and excessive increase of forced convection does not cause a remarkable temperature decrease. This means that there exists an optimum condition for forced convection to control effectively the system in a suitable temperature range without waste of energy.

Temperature uniformity is another important issue that needs to be considered. This can be evaluated quantitatively by examining the standard deviation of the temperature distribution; the result is expressed in Fig. 17. A battery with uniform temperature distribution shows small standard deviation, and vice versa. The standard deviation of the temperature is calculated by the following expression.

$$\mathrm{S.D.} = \sqrt{\frac{\sum_{i=1}^{n} V_i (T_i - T_{\mathrm{avg}})^2}{V_{\mathrm{total}}}} \tag{17}$$

A comparison of the curves A, B, C and D in Fig. 17 shows that the standard deviation increases with enhancing the extent of convection under low to moderate convection. On the other hand, the results surprisingly show that increasing the forced convection does not induce further increase in the standard deviation under strong forced convection, as illustrated by curves E, F. This is because the strong forced convection provides relatively good heat dissipation for the system, and it also narrows the temperature change during operation; thus increasing the temperature uniformity in the system. This result implies that temperature uniformity does not necessarily decrease infinitely when the extent of forced convection is enhanced.

According to the discussion above, the conditions of forced convection should be optimized to obtain a sufficient heat dissipation rate and acceptable temperature uniformity. Since extra energy is needed for forced convection, it is applied if and only if the passive heat dissipation methods do not satisfy the requirements.

3.7. *Effect of contact layer on heat transfer*

The contact layer is generally filled with materials of low thermal conductivity such as liquid electrolytes. It forms a barrier that decreases the heat dissipation performance, but it provides extra heat capacity to mitigate the temperature rise. The interactions of these conflicting factors makes the net effect of contact layer on heat dissipation quite complex. Accordingly, a study has been made of batteries with different thicknesses of contact layer under natural and forced convections at the 3*C* discharge rate. Except for the thickness of the contact layer, the parameters and conditions for each simulation are the same as the default setting. Although the total battery size may vary slightly due to small differences in the thickness of the contact layer, detailed calculation finds that the subtle difference of surface area does not sufficiently affect the total heat dissipation, and can thus be neglected.

The temperature variation and the heat variation (referring to 300 K) of batteries with respect to variations in the thicknesses of the contact layers under natural and forced

Table 8
Heat distribution (referring to 300 K) in lithium battery at end of 3*C* discharge procedure

	Thickness of contact layer (m)					
	Natural convection			Forced convection (h = 100 W m^{-2} K^{-1})		
	0	0.0005	0.001	0	0.0005	0.001
Case (j)	9982.27	9676.61	9346.37	3600.12	3468.69	3378.89
Contact layer (j)	0.00	6702.62	12695.37	0.00	2507.18	5037.85
Core (j)	287603.67	282077.52	278122.04	116556.90	122941.69	128624.93
Total (j)	297585.94	298456.75	300163.78	120157.02	128917.56	137041.67

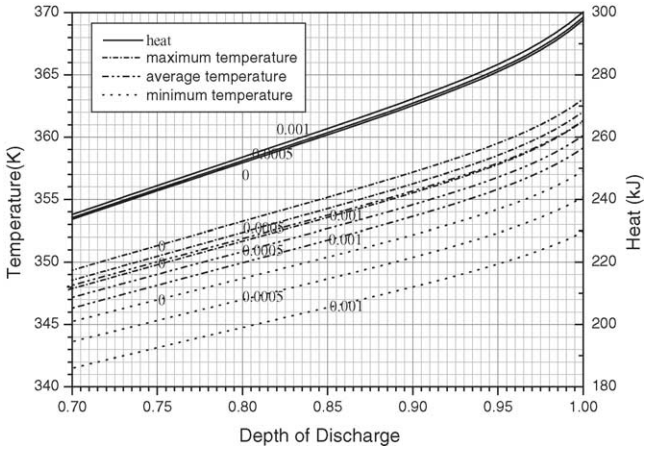

Fig. 18. Temperature variation and heat variation (referring to 300 K) for different thickness of contact layers under natural convection.

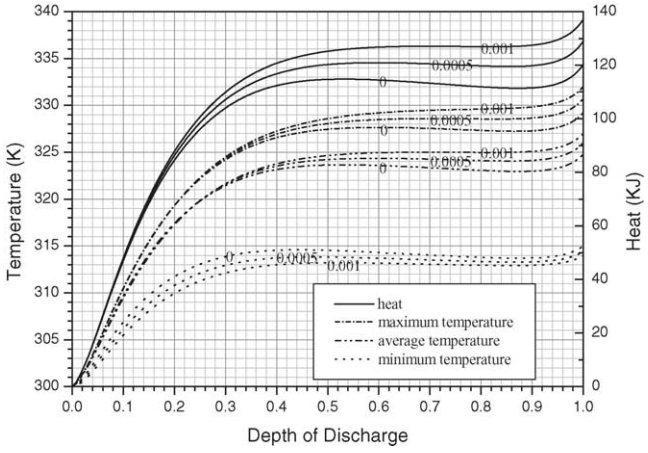

Fig. 19. Temperature variation and heat variation (referring to 300 K) for different thickness of contact layers under forced convection (h = 100 W m^{-2} K^{-1}).

convection are shown in Figs. 18 and 19, respectively. The dashed lines in Fig. 18 show that the temperature decreases with increasing thickness of the contact layer. Natural convection is not sufficiently efficient to dissipate a large amount of heat on the surface to give a shallower temperature gradient inside the battery. Hence, the extra thermal resistance from the contact layer is not a bottleneck for heat transfer, and its extra heat capacity dominates the temperature inside the battery. By contrast, Fig. 19 shows that the extra thermal resistance dominates the temperature, because the strong forced convection dissipates a sufficient amount of heat from the surface, and the extra thermal resistance of the contact layer depresses the efficiency of heat conduction inside a battery. Although the effect of the contact layer on temperature variation depends on the surroundings, it is generally true that batteries with thicker contact layers always retain more heat, as shown in Table 8.

Due to the interaction of these two conflicting factors, it is hard to simplify the calculation of the contact layer by simple expressions. This is why the simplified model, Number 8, over-estimates the surface temperature under natural convection, but under-estimates the surface temperature under forced convection.

4. Conclusions

A detailed three-dimensional thermal model has been developed to simulate the thermal behaviour of a lithium-ion battery. The layer-structured core region, the contact layer and the battery case are all included without simplification. In addition, this model considers the location-dependent convection and the radiation simultaneously to enhance the accuracy at the boundaries. Hence, some important phenomena such as the asymmetric temperature profile and the anomaly of temperature distribution on the surface can be simulated precisely.

Furthermore, a simplified thermal model has been developed for practical application, based on the experience accumulated from the examination of several simplified models. Taking the simulation results from the detailed thermal model as the reference, it can be seen that the battery case and the contact layer are important components, and the complicated core region can be further simplified by adopting the average properties. The simplified model exhibits nearly the same accuracy as the detailed model, but it is about 660 times faster. Even some of the one-dimensional and two-dimensional models could not match the calculation speed of this model.

The simulation results from the detailed thermal model show that the temperature distribution inside the battery is asymmetric. Due to the difference of heat dissipation performance on each surface, the maximum temperature occurs

somewhere below the center of a battery. A close look into the temperature distribution indicates that the heat transfer is greater in *Y*- and *Z*-directions, and the metal case effectively spreads heat on the surface. Furthermore, radiation is found to be an important process for heat dissipation, especially in situations under natural convection. Hence, modifying the surface to enhance the emissivity is an efficient and economic way to improve heat dissipation.

Applying strong forced convection is effective in depressing the maximum temperature inside the battery, but it decreases the temperature uniformity and impairs the battery performance. The simulation results indicate that the temperature uniformity does not decrease infinitely when the extent of forced convection is enhanced. Rather, there is an optimum condition that combines a good heat dissipation rate with acceptable temperature uniformity.

The contact layer forms a barrier to decrease the heat dissipation performance, but it provides extra heat capacity to mitigate the temperature rise. The competition of these conflicting factors makes the net effect of the contact layer on heat dissipation quite complex. The results show that the extra heat capacity dominates the temperature under natural convection, whereas the extra thermal resistance dominates the temperature under forced convection. Hence, the complex roles of the contact layer cannot be ignored.

Acknowledgements

This work has been supported by the Materials Research Laboratories of Industrial Technology Research Institute. The authors would especially like to thank Dr. M.H. Yang for helpful assistance.

References

[1] D. Bernardi, E. Pawlikowski, J. Newman, J. Electrochem. Soc. 132 (1985) 5.
[2] Y. Chen, J.W. Evans, J. Electrochem. Soc. 140 (1993) 1833.
[3] Y. Chen, J.W. Evans, J. Electrochem. Soc. 141 (1994) 2947.
[4] Y. Chen, J.W. Evans, J. Electrochem. Soc. 143 (1996) 2708.
[5] J. Lee, K.W. Choi, N.P. Yoo, C.C. Christianson, J. Electrochem. Soc. 133 (1986) 1286.
[6] C.R. Pals, J. Newman, J. Electrochem. Soc. 142 (1995) 3274.
[7] C.R. Pals, J. Newman, J. Electrochem. Soc. 142 (1995) 3282.
[8] L. Song, J.W. Evans, J. Electrochem. Soc. 147 (2000) 2086.
[9] G.N. Ellison, Thermal Computations for Electronic Equipment, Van Nostrand Reinhold, New York, 1969.
[10] W.B. Gu, C.Y. Wang, J. Electrochem. Soc. 147 (2000) 2910.
[11] G.G. Botte, V.R. Subramanian, R.E. White, Electrochim. Acta 45 (2000) 2695.
[12] G.F. Hewitt, G.L. Shires, T.R. Bott, Process Heat Transfer, CRC Press, London, 1993.
[13] D.A. Patterson, J.L. Hennessy, Computer Organization and Design, 2nd ed., Morgan Kaufmann Publishers Inc., San Francisco, 1997.